Science Advances
AAAS

Manuscript Template

Title

Validation of Microscopic Magneto-Chiral Dichroism Theory

Authors

M. Atzori,[1,$] H. D. Ludowieg,[2,$] Á. Valentín-Pérez,[3,4,+] ,M. Cortijo,[3,4,5] I. Breslavetz,[1] K. Paillot,[1] P. Rosa,[3] C. Train,[1] J. Autschbach,[2,#] E. A. Hillard,[3,4] G. L. J. A. Rikken[1*]

Affiliations

1. Laboratoire National des Champs Magnétiques Intenses (LNCMI), Univ. Grenoble Alpes, INSA Toulouse, Univ. Paul Sabatier, EMFL, CNRS, Toulouse & Grenoble, France
2. Department of Chemistry, University at Buffalo, State University of New York, Buffalo, New York 14260, United States
3. CNRS, Univ. Bordeaux, Bordeaux INP, ICMCB, UMR 5026, F-33600 Pessac, France
4. Univ. Bordeaux, CNRS, Centre de Recherche Paul Pascal, UMR5031, 33600 Pessac, France
5. Current address: Departamento de Química Inorgánica, Facultad de Ciencias Químicas, Universidad Complutense de Madrid, Ciudad Universitaria, E-28040 Madrid, Spain

* corresponding author : geert.rikken@lncmi.cnrs.fr
\# corresponding author : jochena@buffalo.edu

$ these authors have contributed equally to the work

\+ deceased

Abstract

Magneto-chiral dichroism (MChD), a fascinating manifestation of the light-matter interaction characteristic for chiral systems under magnetic fields, has become a well-established optical phenomenon reported for many different materials. However, its interpretation remains essentially phenomenological and qualitative, because the existing microscopic theory has not been quantitatively confirmed by confronting calculations based on this theory with experimental data. Here we report the experimental low-temperature MChD spectra of two archetypal chiral paramagnetic crystals taken as model systems, *tris*(1,2-diaminoethane)nickel(II) and cobalt(II) nitrate, for light propagating parallel or perpendicular to the *c* axis of the crystals, and the calculation of the MChD spectra for the Ni(II) derivative by state-of-the-art quantum chemical calculations. By incorporating vibronic coupling, we find a good agreement between experiment and theory, which opens the way for MChD to develop into a powerful chiral spectroscopic

tool and provide fundamental insights for the chemical design of new magneto-chiral materials for technological applications.

Introduction

More than 200 years ago, Arago discovered the rotation of light polarization in chiral quartz crystals.(*1*) Inspired by Faraday's discovery of the apparently similar magnetically-induced optical rotation,(*2*) Pasteur tried, unsuccessfully, to induce chirality in crystals by growing them under a magnetic field.(*3*) Over the years, subsequent attempts at using a magnetic field to induce chirality have all failed.(*4*) This is because chirality and magnetic fields correspond to the breaking of two different fundamental symmetries, mirror symmetry and time-reversal symmetry respectively, and have no direct link.

Nonetheless, an effect that corresponds to the simultaneous breaking of both symmetries does exist. It was first predicted to take the form of a difference in absorption and refractive index for unpolarized light traversing the chiral medium parallel or antiparallel to an applied magnetic field (***B***), and to be of opposite sign for the two enantiomers.(*5–7*) The prediction of this fundamental interaction, named Magneto-Chiral Dichroism (MChD),(*8*, *9*) was experimentally validated in 1997.(*10*) It has been used to photochemically favor one of the two enantiomers of a racemic mixture in a magnetic field with unpolarized light,(*11*) thus providing a possible mechanism for the homochirality of life.(*12*, *13*) Since then, MChD has been observed across the whole electromagnetic spectrum from X-rays(*14*, *15*) to microwaves,(*16*) for dia-, para- and ferromagnetic chiral materials.(*17*, *18*) Magneto-chirality has also been generalized to other domains, like electrical conductivity(*19*, *20*) and sound propagation,(*21*) underlining the universality of this effect. Magneto-chiral effects, being intrinsically non-reciprocal, have also raised a large interest in the context of topological materials, like Weyl semi-metals(*22*) and in all materials with a strong spin-orbit coupling.(*23*)

The microscopic theory for the Faraday effect and magnetic circular dichroism (MCD) was one of the early successes of quantum mechanics,(*24–26*) yielding an expression for the difference Δn between the complex refractive indices of the medium for left- and right-circularly polarized light propagating parallel to a static magnetic field ***B*** of the form

$$\Delta n_{MCD}(\omega, \boldsymbol{B}) \propto B\big(\mathrm{A} \cdot f(\omega) + (\mathrm{B} + \mathrm{C}/kT) g(\omega)\big) \quad (1)$$

where ω is the frequency of the light and f and g are dispersive and absorptive line shape functions, respectively. The different terms on the right-hand side of equation 1 can be associated with different effects of the magnetic field on the electronic system; the lifting of degeneracy of ground- or excited-state levels (A term), the mixing of electronic wavefunctions (B term) and the change in the population of formerly degenerate ground-state levels (C term). This well-established theory has allowed MCD to develop into a powerful spectroscopic technique,(*27*) applied to a large range of systems in physics, chemistry and biology, ranging from atoms to metalloenzymes, leading to the industrial development of magneto-optical media for data storage.

Barron and Vrbancich (BV) developed the corresponding microscopic theory for MChD, resulting in an analogous expression for the difference Δn_{MChD} between the complex refractive indices of the medium for unpolarized light propagating parallel or antiparallel to the field,(*8*) of the form

$$\Delta n_{MChD}^{\mathrm{D/L}}(\omega,\boldsymbol{k},\boldsymbol{B}) \propto \boldsymbol{k}\cdot\boldsymbol{B}\left\{\mathrm{A}_1^{\mathrm{D/L}}\cdot f_1(\omega)+\left(\mathrm{B}_1^{\mathrm{D/L}}+\mathrm{C}_1^{\mathrm{D/L}}/kT\right)g_1(\omega)+\mathrm{A}_2^{\mathrm{D/L}}\cdot f_2(\omega)+\left(\mathrm{B}_2^{\mathrm{D/L}}+\mathrm{C}_2^{\mathrm{D/L}}/kT\right)g_2(\omega)\right\} \quad (2)$$

where for all $X^{\mathrm{D/L}}$ terms $X^{\mathrm{D}} = -X^{\mathrm{L}}$, i.e., they change sign with the handedness of the medium (D, dextro and L, laevo). The X_1 terms correspond to electric dipole-magnetic dipole contributions whereas the X_2 terms correspond to electric dipole-electric quadrupole contributions and the same magnetic field effects outlined above for MCD underlie the different A, B and C terms in MChD.

Although MChD has now been experimentally observed in different types of materials, no quantitative comparison of experimental results with the microscopic BV theory has been made so far. From the experimental side, the determination of accurate MChD spectra in the presence of the generally much stronger natural circular dichroism (NCD) and MCD effects is challenging. Some MChD calculations, based on the BV theory, have been reported for small molecules, but they have not been compared to experiments, the predicted values being beyond current experimental sensitivity.(*28*)

In order to bring our quantitative understanding of MChD to the same level as that of NCD and MCD, and to underpin the potential of MChD as a chiral spectroscopy tool, we have selected two well-characterized paramagnetic chiral materials, with clearly identified optical transitions, *tris*(1,2-diaminoethane)metal(II) nitrate $[M^{II}(dae)_3](NO_3)_2$ ($M^{II} = Ni^{2+}$ (**1**), Co^{2+} (**2**); dae = 1,2-diaminoethane). These tris-chelated octahedral enantiopure complexes (Figure 1) are obtained by spontaneous resolution during crystallization and crystallize in the chiral $P6_322$ space group. Below 109 K, the two enantiomers of **1** undergo a reversible phase transition in two enantiomorphic space groups, namely $P6_122$ for **1-Λ** and $P6_522$ for **1-Δ**,(*29*) while the two enantiomers of **2** maintain the $P6_322$ space group down to 4 K.(*30*) The magnetic properties of **1** and **2** have been recently investigated, revealing a typical paramagnetic behavior of octahedral d^n (n = 7, 8) metal ions with a moderate to high axial zero-field splitting for the nickel(II) and cobalt(II) derivatives, respectively.(*30*)

We have measured their low temperature absorption and MChD spectra in the 4 K–16 K range, both parallel and perpendicular to the optical axis. In this temperature range, the experimental MChD spectra turn out to be entirely dominated by the C_i terms (Eq. 2), identified by their temperature dependence, thereby greatly reducing the computational effort required to calculate the spectrum and increasing the accuracy of the results.

The BV theory expresses the electric dipole-magnetic dipole C_1 term and the electric dipole-electric quadrupole C_2 term of Eq. 2 as a sum over transition moments between the electronic wavefunctions of the ions, perturbed by their ligands. We have calculated these transition moments, including the vibronic coupling contributions, for the Ni(II) derivative with state-of-the-art quantum chemical methods, using optimized geometries based on experimental X-ray structures.

Results

Magneto-Chiral Dichroism measurements. MChD measurements were performed in the 440–1100 nm spectral window on single crystals of **1-Λ**, **1-Δ** and **2-Λ**, **2-Δ** and the light wavevector ***k*** parallel to the magnetic field, the *c* crystallographic axis aligned parallel (axial) or perpendicular (orthoaxial) to the magnetic field, in the temperature range 4.0–16.0 K (Figure 2).

Figures 2a and 2b show the MChD spectra $\Delta A_{MChD} \equiv (A(\boldsymbol{B} \uparrow\downarrow k) - A(\boldsymbol{B} \uparrow\uparrow k)/\boldsymbol{B}$ with the magnetic field $\boldsymbol{B}$ and light wavevector $\boldsymbol{k}$ orthogonal to the c crystallographic axis for the two enantiomers of **1** and **2**, respectively, for several temperatures. MChD spectra with equal intensity and opposite signs for the two enantiomers are obtained. **1** shows a strong MChD signal composed of two contributions centered at λ = 840 and 965 nm, respectively, and a very weak contribution around 520 nm. **2** shows three strong MChD signals centered at λ = 474 nm, 532 nm and 960 nm, the lowest energy contribution being the most intense. The intensity of the various MChD signals, for both **1** and **2**, varies linearly with the inverse of the temperature and linearly with the magnetic field strength, as illustrated by the insets of Figure 2a and Figure 2b. The observed $1/T$ temperature dependence of the MChD strength confirms the dominance of the C terms of the BV theory. The calculations show that for this case, the electric dipole – magnetic dipole contribution dominates, i.e., $C_1 >> C_2$.

MChD measurements were also performed with the magnetic field $\boldsymbol{B}$ and light wavevector $\boldsymbol{k}$ parallel to the c crystallographic axis for the Δ enantiomer of **1**. As shown in Figure 3a, the MChD spectra for **1** highly depend on the relative orientation of $\boldsymbol{k}$ and c. The two contributions of the strong MChD signal of **1** have the same sign in the orthoaxial configuration whereas they are of opposite sign in the axial configuration (Figure 3a). Moreover, two weak MChD signals at λ = 730 and 780 nm are better evidenced in the axial configuration.

Magneto-Chiral Dichroism calculations. The results of the calculations of the MChD spectrum for **1** for both axial and orthoaxial orientations are shown in Figure 3b, with and without the vibronic coupling. Very good agreement with the experimental MChD spectra is obtained only when the vibronic coupling is included. Although the ligand-field transitions are not Laporte forbidden in D_3 symmetry, the local distortions from the octahedral parent symmetry around the metal ion are not large, and consequently the purely electronic contributions to the MChD spectrum are minor. Note that substantial deviations from experimental intensities are not uncommon in the quantum theoretical modeling of spectra, and expected, given the approximations (see SI) that were necessary in the computational model for the complex (the BV equations themselves were not approximated further). Figures S1 and S2 in the Supplementary Material show that the experimental relative band intensities of the orthoaxial absorption spectra and NCD spectra shown in Figure 2c, and the experimental absorption spectra for axial and orthoaxial light propagation,(*31*) are also correctly reproduced by our calculations (albeit with overall too high intensity), which further validates the theoretical approach.

Discussion

Compounds **1** and **2** show particularly strong MChD signals resulting from specific electronic *d-d* transitions falling in the Vis-NIR spectral window whose intensity is mainly associated to electric-dipole and vibronic contributions of the D_3 molecular symmetry group.[26–28]

By referring to the electronic spectrum of **1** ($^3A_2$ ground state, Figure 2c), it appears that the strongest MChD signals are associated to the absorption band centered at λ = 853 nm (orange line in Figure 2c) which is assigned to the spin-allowed $^3T_2(^3F) \leftarrow {}^3A_2(^3F)$ transition. Under D_3 symmetry, the $^3T_2$ term splits in the $^3A_1$ + ^3E terms. Such splitting, that does not allow to experimentally distinguish two separate absorption bands, is associated to two separate MChD signals, the lowest in energy changing sign upon passing from the orthoaxial to the axial configuration. The strong intensity of these two

MChD signals can be associated with the electric dipole and vibronic allowed character of both $^3A_1 \leftarrow {}^3A_2$ and $^3E \leftarrow {}^3A_2$ electronic transitions, and the magnetic dipole allowed character of the parent $^3T_2(^3F) \leftarrow {}^3A_2(^3F)$ transition, which is reflected by its high natural circular dichroism (NCD) (dashed lines in Figure 2c).
The absorption spectrum of **1** shows an absorption band at λ = 780 nm (green line in Figure 2c) as a shoulder to the λ = 853 nm band, which is assigned to the $^1E(^1D) \leftarrow {}^3A_2(^3F)$ spin forbidden transition. This band, which is clearly identified by spectral deconvolution of the absorption spectrum (Figure 2c), provides a low contribution to the MChD spectrum, which is convoluted in the broader and stronger MChD signal resulting from the lower energy absorption. Accordingly, this spin-forbidden transition only weakly contributes to the NCD.

The weak MChD observed in the 500-600 nm spectral region is instead associated to the intense absorption at λ = 530 nm (magenta line in Figure 2c), which is assigned to the $^3T_1(^3F) \leftarrow {}^3A_2(^3F)$ spin-allowed electronic transition. Under D_3 symmetry the $^3T_1$ term splits into the $^3A_2 + {}^3E$ terms. Only the $^3E \leftarrow {}^3A_2$ component is electric dipole allowed (σ or *xy* polarized) but the experimental observation of a quite intense and broad band also in the spectrum recorded with ***k*** parallel to the *c* axis (axial configuration, π or *z* polarization) suggests that this band is mainly vibronic in nature.(*31*) Its MChD intensity is weak, although non-zero, in agreement with the magnetic dipole forbidden character of this transition, while its non-zero NCD has been associated to the mixing of the ^3E states in a trigonal ligand field.

Finally, the absorption at λ = 468 nm (blue line), which is assigned to the $^1A_1(^1G) \leftarrow {}^3A_2(^3F)$ spin-forbidden electronic transition, does not provide a detectable MChD signal, in agreement with is negligible contribution to the NCD. This electronic transition gains intensity by mixing through spin-orbit coupling with nearby spin-allowed transitions. Prior density functional calculations of the absorption and NCD spectrum have confirmed these considerations and identified the motion of the first-coordination sphere $[NiN_6]$ unit as the main source of vibronic coupling when compared to the complex periphery.(*32*)

The MChD signals of **2** are associated to its $^4T_1$ ground state electronic spectrum (Figure 2d).(*33*) The strongest MChD signal is associated to the absorption at λ = 960 nm (orange line) which is assigned to the $^4T_2(^4F) \leftarrow {}^4T_1(^4F)$ spin-allowed electronic transition, which is electric dipole allowed. However, the temperature dependence of its intensity suggests significant vibronic effects.(*31*) The high MChD response is in agreement with the magnetic-dipole allowed character of this transition, which also results in a high NCD response.

The sharp and intense MChD signal at λ = 532 nm (green line in Figure 2c) is associated to the $^2T_1(^4P) \leftarrow {}^4T_1(^4F)$ spin-forbidden electronic transition. This spin-forbidden band is associated to a high spin-orbit coupling character, which explains its comparable intensity with spin-allowed transitions both in terms of electronic absorption and MChD, considering its intrinsically lower rotational strength.(*31*, *34*)

Finally, an additional strong MChD signal is found at λ = 474 nm and associated to the $^4T_1(^4P) \leftarrow {}^4T_1(^4F)$ spin-allowed electronic transition (magenta line in Figure 2c). As for the $^4T_2(^4F) \leftarrow {}^4T_1(^4F)$ transition, this electric dipole allowed transition shows significant vibronic effects and, being magnetic dipole allowed, shows a high NCD response.

Overall, these results are in very good agreement with the nature of the originating electronic transitions, their intrinsic rotary strength, and the spin-orbit coupling character. This is highlighted by the stronger MChD signal associated to the $^4T_2 \leftarrow {}^4T_1$ transition of **2** with respect to the $^3T_2 \leftarrow {}^3A_2$ transition of **1** although the rotatory strength is lower, and by the high MChD intensity of the spin-forbidden $^2T_1 \leftarrow {}^4T_1$ transition of **2**, with respect to the $^1E \leftarrow {}^3A_2$ of **1**. However, the impact of the vibronic coupling on MChD signals remains difficult to evaluate exclusively from experimental data.

The calculations for **1** confirm the assignments of the electronic states underlying the observed spectral bands. Without vibronic coupling, the calculated spectra (Figure 3b) are in strong disagreement with the experimental spectra. On the contrary, when vibronic coupling contributions are included in the calculations, they agree very well in shape and intensity with the experimental ones for both orthoaxial and axial configurations. This crucial influence of vibronic coupling is reinforced when considering the high energy part of the spectra: the MChD contributions associated to the vibronic band in the 500-550 nm range (calculated) and observed at slightly lower energies (520-600 nm) appear only when the vibronic coupling contribution is included in the calculations, in agreement with the experimental assignments. The calculated intensity and the shape of these signals are not accurately reproduced in the experiments most probably because even a slight mis-orientation of the crystal leads to mixing of axial and orthoaxial contributions of opposite sign.

The calculations thereby confirm the long-standing assumptions(*31*) that most of the intensity of the ligand-field spectrum of these materials is not purely electronic, but mostly vibronic. Interestingly, when the vibronic coupling (VC) contributions are included, the absorption spectrum (Figure S2) is not strongly anisotropic—in agreement with the experiments—but the MChD spectrum clearly is. In the intense, long-wavelength part of the spectrum, VC not only strongly enhances the intensity of all the bands, it also correctly flips the sign of the 853 nm band. The calculations also show that the MChD *C* term vanishes in the absence of spin-orbit coupling (SOC), which is analogous to the MCD *C* term for orbitally non-degenerate ground states, and that the contributions from the electric quadrupole transition moments (i.e. C_2) are negligible. Unfortunately, we had to postpone attempts to calculate the vibronic MChD spectrum of **2** because of severe computational scaling issues caused by the large number of spin doublet states needed for the combination of VC and SOC. Results for **2** and other systems will be presented in follow-up studies.

To provide quantitative information about the MChD in these compounds, we exploited the anisotropy factor $g_{MChD} \equiv (2\,\Delta A_{MChD}/A)\,/B$, whose values are summarized in Table 1. It should be highlighted that the absence of a clear separation between the $^3A_1 \leftarrow {}^3A_2$ and $^3E \leftarrow {}^3A_2$ absorptions for **1** and their superposition with the spin-forbidden transition centered at $\lambda = 780$ nm do not allow to accurately calculate g_{MChD} for these transitions and the values reported in Table 1 should thus be considered only as an estimate. For **2,** g_{MChD} values can be determined unequivocally, and these will be discussed below.

Overall, the g_{MChD} values of **2** follow the trend observed for the g_{NCD} values that can be estimated from the literature data (Figure 2) of ca. 0.58, 1.54, 1.34, for the highest to the lowest energy absorptions, respectively. The values of g_{MChD} are remarkably high for the $^4T_2(^4F) \leftarrow {}^4T_1(^4F)$ and $^2T_1(^4P) \leftarrow {}^4T_1(^4F)$ transitions of the octahedral Co(II) metal center, being of the order of ca. 0.20 T^{-1}. On the basis of the theoretical calculations performed on

the Ni(II) derivative, the origin of the gain in intensity for these two signals can be deduced: the lowest energy contribution most likely gains intensity because it is associated to a high vibronic and magnetic-dipole character of its electronic transition (*see above*),(*31*) while the signal associated to the spin-forbidden transition gains intensity thanks to its high SOC,(*31*, *34*) the two fundamental ingredients that are required to theoretically reproduce the experimental data.

It is informative to compare these g_{MChD} values with those reported in the literature. They are higher than those recently observed, for the most MChD active transitions of a magnetically ordered molecular canted antiferromagnet based on a octahedrally Mn(III) ions, axially elongated by a Jahn-Teller distortion (g_{MChD} = 0.12 at magnetic saturation).(*35*) As **2** is a simple paramagnet, our results indicate that even larger magneto-chiral anisotropies may be obtained if enantiopure Co(II) centers are introduced in a magnetically ordered system to take advantage of the proportionality between the MChD and the magnetization of the system.(*17*) Larger MChD can also be expected for paramagnetic metal centers with larger SOC, like the second and third row transition metals or lanthanides and actinides. These results also suggest that the "structural ingredient" that permits the observation of such strong MChD signals is the first-coordination sphere metal-centered helical chirality of the chromophore, a structural feature that has been rarely encountered so far in the molecular compounds investigated for their MChD response.(*36*) Indeed, although it has been demonstrated that strong MChD signals can also be observed by introducing second coordination sphere chiral features,(*35*, *37*), the MChD response is stronger in the presence of first coordination sphere chiral features.

In summary, we have experimentally and theoretically investigated the magneto-chiral dichroism of two model systems, *tris*(1,2-diaminoethane)nickel(II) and its cobalt(II) analogue. Very strong MChD signals have been experimentally observed and associated with the metal ions' absorption bands. Their temperature dependence is characteristic for C terms in the BV theory. Good agreement is found with calculations of such C terms, thereby confirming for the first time this part of the BV theory.
The role of crystalline anisotropy in MChD is highlighted both in our experiments and calculations. These results identify the fundamental role of vibronic coupling in the overall intensity and shape of the MChD spectrum of transition metal complexes apart from the already recognized role of spin-orbit coupling. Clearly, the combination of metal-centered helical chirality and slight octahedral distortion of the D_3 symmetry induces the right deviation from non-centrosymmetry that enables a strong MChD effect through vibronic coupling, as demonstrated by state-of-art MChD theoretical calculations.

Materials and Methods

Materials preparation and characterization. Compounds **1** and **2** are obtained by reaction of the *dae* ligand with the respective nitrate metal ion salts under dry nitrogen or argon using standard glovebox or Schlenk techniques, according to published procedures. (*30*, *31*, *33*, *34*) Crystallization provides in both cases hexagonal-shaped single crystals elongated along the *c* axis of typical 4.0 x 2.0 x 2.0 mm dimensions. X-ray diffraction analysis has been used to verify the crystal structure and the absolute configuration of each measured single crystal. Typical Flack parameters were 0.006(8), 0.01(5), 0.005(5) and -0.001(7).

Magneto-chiral dichroism spectroscopy. MChD spectra were recorded with a home-made multichannel MChD spectrometer operating in the visible and near infrared spectral

window (420-1600 nm) between 4.0 and 300 K with an alternating magnetic field ***B*** up to 2.0 T amplitude. A detailed description of the measurement apparatus has been reported elsewhere.(*38*)

Magneto-chiral dichroism calculations. The BV theory expresses the electric dipole-magnetic dipole C_1 term and the electric dipole-electric quadrupole C_2 term of Eq. 2 as

$$\begin{aligned} C_1 &= \frac{1}{d}\sum_{\alpha,\beta,\gamma}\epsilon_{\alpha,\beta,\gamma}\sum_{n} m_{n,n}^{\alpha}\,\mathrm{Re}\left[\mu_{n,j}^{\beta} m_{j,n}^{\gamma}\right] \\ C_2 &= \frac{\omega}{15d}\sum_{\alpha,\beta}\sum_{n} m_{n,n}^{\alpha}\,\mathrm{Im}\left[3\mu_{n,j}^{\beta}\Theta_{j,n}^{\beta,\alpha} - \mu_{n,j}^{\alpha}\Theta_{j,n}^{\beta,\beta}\right] \end{aligned}$$

Here, d is the degeneracy of the ground state (GS), n represents one of the components of the GS, j is an excited state that may or may not be a component of a degenerate level, $m_{n,j}^{\alpha}, \mu_{n,j}^{\alpha}$, and $\Theta_{n,j}^{\alpha,\beta}$ are matrix elements of the Cartesian components α, β, γ of the magnetic dipole moment, the electric dipole moment, and the traceless quadrupole moment operators, respectively, and $\epsilon_{\alpha,\beta,\gamma}$ is the Levi-Civita tensor. The BV theory was developed for an isotropic ensemble of arbitrarily oriented molecules and the expression above represents an average over the rotations of the molecule relative to an arbitrary fixed direction of the static magnetic field. The Cartesian index α of $m_{n,n}^{\alpha}$, defines the direction of the static field, which is averaged over in the previous expressions. Therefore, the MChD intensity for light propagation along direction α, parallel to the magnetic field, and relative to a fixed molecular orientation, must be given by three times the contribution from $m_{n,n}^{\alpha}$, in the isotropic MChD equation.

For the calculations, we determined the excitation frequencies and the complex transition moment matrix elements from relativistic multi-reference wave function calculations with SOC, using a developer's version of OpenMolcas(*39*) as explained in the Supplementary Material. The C_i were determined from the wave function data for a pre-set absolute temperature, using a code developed in-house as an extension of a previous development for MCD C term calculations from the same type of wave function data.(*40*, *41*) The extensions comprised the ability to calculate MChD for purely electronic transitions as well as the capability for generating the corresponding vibronic transitions and their associated moments. The resulting data were then multiplied by the line shape functions of the BV theory, using an empirical level broadening Γ of 0.003 Hartree (658 cm^{-1}) for the transitions. In reference to Eq. (2), the line shape functions are given as

$$g_1(\omega) = \omega_j \frac{\omega\Gamma_j}{(\omega_j^2-\omega^2)^2+\omega^2\Gamma_j^2} \;\; ; \;\; g_2(\omega) = -\omega \frac{\omega\Gamma_j}{(\omega_j^2-\omega^2)^2+\omega^2\Gamma_j^2}$$

for a resonant transition with circular transition frequency ω_j.

The theoretical methods for calculating Herzberg-Teller vibronic absorption spectra within the chosen methodological framework have been introduced elsewhere,(*42–44*) and were generalized for the present MChD calculations. See the Supplementary Information for further details.

References and Notes

1. J.B. Biot, Mémoire sur une modification remarquable qu'éprouvent les rayons lumineux dans leur passage à travers certains corps diaphanes, et sur quelques autres nouveaux phénomènes d'optique. *Mémoires la Cl. des Sci. mathématiques Phys. l'Institut Impérial Fr.*, 93–134 (1812).
2. Faraday M., I. Experimental researches in electricity.—Nineteenth series. *Philos. Trans. R. Soc. London*. **136**, 1–20 (1846).
3. L. Pasteur, Relation qui peut exister entre la forme crystalline et la composition chimique sur las cause de la polarization rotatoire. *C. R. Acad. Sci. Paris*. **26**, 535–539 (1848).
4. B. L. Feringa, R. A. van Delden, Absolute Asymmetric Synthesis: The Origin, Control, and Amplification of Chirality. *Angew. Chemie Int. Ed.* **38**, 3418–3438 (1999).
5. G. Wagnière, A. Meier, The influence of a static magnetic field on the absorption coefficient of a chiral molecule. *Chem. Phys. Lett.* **93**, 78–81 (1982).
6. M. P. Groenewege, A theory of magneto-optical rotation in diamagnetic molecules of low symmetry. *Mol. Phys.* **5**, 541–563 (1962).
7. Y. Mulyana, K. Ishii, A novel aspect of spectroscopy for porphyrinic compounds under magnetic fields. *Dalt. Trans.* **43**, 17596–17605 (2014).
8. L. D. Barron, J. Vrbancich, Magneto-chiral birefringence and dichroism. *Mol. Phys.* **51**, 715–730 (1984).
9. L. D. Barron, *Molecular Light Scattering and Optical Activity* (Cambridge University Press, 2004).
10. G. L. J. A. Rikken, E. Raupach, Observation of magneto-chiral dichroism. *Nature*. **390**, 493–494 (1997).
11. E. Raupach, G. L. J. A. Rikken, C. Train, B. Malézieux, Modelling of magneto-chiral enantioselective photochemistry. *Chem. Phys.* **261**, 373–380 (2000).
12. G. Wagnière, A. Meier, Difference in the absorption coefficient of enantiomers for arbitrarily polarized light in a magnetic field: A possible source of chirality in molecular evolution. *Experientia*. **39**, 1090–1091 (1983).
13. L. D. Barron, False Chirality, Absolute Enantioselection and CP Violation: Pierre Curie's Legacy. *Magnetochemistry*. **6**, 5 (2020).
14. R. Sessoli, M.-E. Boulon, A. Caneschi, M. Mannini, L. Poggini, F. Wilhelm, A. Rogalev, Strong magneto-chiral dichroism in a paramagnetic molecular helix observed by hard X-rays. *Nat. Phys.* **11**, 69–74 (2015).
15. M. Ceolín, S. Goberna-Ferrón, J. R. Galán-Mascarós, Strong Hard X-ray Magneto-Chiral Dichroism in Paramagnetic Enantiopure Molecules. *Adv. Mater.* **24**, 3120–3123 (2012).
16. S. Tomita, K. Sawada, H. Kurosawa, T. Ueda, in *Springer Series in Materials Science* (2019).
17. M. Atzori, G. L. J. A. Rikken, C. Train, Magneto-Chiral Dichroism: A Playground for Molecular Chemists. *Chem. – A Eur. J.* **26**, 9784–9791 (2020).
18. K. Ishii, S. Hattori, Y. Kitagawa, Recent advances in studies on the magneto-chiral dichroism of organic compounds. *Photochem. Photobiol. Sci.* **19**, 8–19 (2020).
19. G. L. J. A. Rikken, J. Fölling, P. Wyder, Electrical Magnetochiral Anisotropy. *Phys. Rev. Lett.* **87**, 236602 (2001).
20. F. Pop, P. Auban-Senzier, E. Canadell, G. L. J. A. Rikken, N. Avarvari, Electrical magnetochiral anisotropy in a bulk chiral molecular conductor. *Nat. Commun.* **5**, 3757 (2014).
21. T. Nomura, X.-X. Zhang, S. Zherlitsyn, J. Wosnitza, Y. Tokura, N. Nagaosa, S. Seki, Phonon Magnetochiral Effect. *Phys. Rev. Lett.* **122**, 145901 (2019).
22. T. Morimoto, N. Nagaosa, Chiral Anomaly and Giant Magnetochiral Anisotropy in

Noncentrosymmetric Weyl Semimetals. *Phys. Rev. Lett.* **117**, 146603 (2016).
23. G. Chang, B. J. Wieder, F. Schindler, D. S. Sanchez, I. Belopolski, S.-M. Huang, B. Singh, D. Wu, T.-R. Chang, T. Neupert, S.-Y. Xu, H. Lin, M. Z. Hasan, Topological quantum properties of chiral crystals. *Nat. Mater.* **17**, 978–985 (2018).
24. R. Serber, The Theory of the Faraday Effect in Molecules. *Phys. Rev.* **41**, 489–506 (1932).
25. W. P. Healy, The multipole Hamiltonian and magnetic circular dichroism. *J. Chem. Phys.* **64**, 3111 (1976).
26. D. P. Craig, T. Thirunamachandran, *Molecular Quantum Electrodynamics* (Dover, New York, New York, USA, 1998).
27. W. R. Mason, *A Practical Guide to Magnetic Circular Dichroism Spectroscopy* (John Wiley & Sons, Inc., Hoboken, NJ, USA, 2007).
28. J. Cukras, J. Kauczor, P. Norman, A. Rizzo, G. L. J. A. Rikken, S. Coriani, A complex-polarization-propagator protocol for magneto-chiral axial dichroism and birefringence dispersion. *Phys. Chem. Chem. Phys.* **18**, 13267–13279 (2016).
29. L. J. Farrugia, P. Macchi, A. Sironi, Reversible displacive phase transition in $[Ni(en)_3]^{2+}$ $(NO^{3-})_2$: a potential temperature calibrant for area-detector diffractometers. *J. Appl. Crystallogr.* **36**, 141–145 (2003).
30. M. Cortijo, Á. Valentín-Pérez, M. Rouzières, R. Clérac, P. Rosa, E. A. Hillard, Tris(ethylenediamine) Cobalt(II) and Manganese(II) Nitrates. *Crystals*. **10**, 472-486 (2020).
31. R. Dingle, R. A. Palmer, The source of spectral band intensity in tris ethylenediamine complexes. *Theor. Chim. Acta*. **6**, 249–256 (1966).
32. A. J. Bridgeman, B. Courcot, T. Nguyen, Modelling the circularly and linearly polarised spectrum of [Ni(en)3]2+. *Dalt. Trans.* **41**, 5362–5367 (2012).
33. M. C. L. Yang, R. A. Palmer, Natural solid state optical activity of tris(ethylenediamine)metal(II) nitrates. II. Single-crystal circular and linear dichroism spectra of tris(ethylenediamine)cobalt(II) nitrate. *J. Am. Chem. Soc.* **97**, 5390–5395 (1975).
34. M. C.-L. Yang, R. A. Palmer, The Natural Optical Activity of Tris(Ethylenediamine)Metal(II) Nitrates V. The Single Crystal Circular Dichroism Spectrum of $Ni(en)_3(NO_3)_2$. *J. Chinese Chem. Soc.* **25**, 195–201 (1978).
35. M. Atzori, F. Santanni, I. Breslavetz, K. Paillot, A. Caneschi, G. L. J. A. Rikken, R. Sessoli, C. Train, Magnetic Anisotropy Drives Magnetochiral Dichroism in a Chiral Molecular Helix Probed with Visible Light. *J. Am. Chem. Soc.* **142**, 13908–13916 (2020).
36. C. Train, R. Gheorghe, V. Krstic, L.-M. Chamoreau, N. S. Ovanesyan, G. L. J. A. Rikken, M. Gruselle, M. Verdaguer, Strong magneto-chiral dichroism in enantiopure chiral ferromagnets. *Nat. Mater.* **7**, 729–734 (2008).
37. M. Atzori, I. Breslavetz, K. Paillot, K. Inoue, G. L. J. A. Rikken, C. Train, A Chiral Prussian Blue Analogue Pushes Magneto-Chiral Dichroism Limits. *J. Am. Chem. Soc.* **141**, 20022–20025 (2019).
38. G. Kopnov, G. L. J. A. Rikken, A multichannel magneto-chiral dichroism spectrometer. *Rev. Sci. Instrum.* **85**, 053106 (2014).
39. I. Fdez. Galván, M. Vacher, A. Alavi, C. Angeli, F. Aquilante, J. Autschbach, J. J. Bao, S. I. Bokarev, N. A. Bogdanov, R. K. Carlson, L. F. Chibotaru, J. Creutzberg, N. Dattani, M. G. Delcey, S. S. Dong, A. Dreuw, L. Freitag, L. M. Frutos, L. Gagliardi, F. Gendron, A. Giussani, L. González, G. Grell, M. Guo, C. E. Hoyer, M. Johansson, S. Keller, S. Knecht, G. Kovačević, E. Källman, G. Li Manni, M. Lundberg, Y. Ma, S. Mai, J. P. Malhado, P. Å. Malmqvist, P. Marquetand, S. A. Mewes, J. Norell, M. Olivucci, M. Oppel, Q. M. Phung, K. Pierloot, F. Plasser, M. Reiher, A. M. Sand, I. Schapiro, P. Sharma, C. J. Stein, L. K. Sørensen, D. G. Truhlar, M. Ugandi, L. Ungur, A. Valentini, S. Vancoillie, V. Veryazov, O. Weser, T. A. Wesołowski, P.-O. Widmark, S. Wouters, A. Zech, J. P. Zobel, R. Lindh,

OpenMolcas: From Source Code to Insight. *J. Chem. Theory Comput.* **15**, 5925–5964 (2019).

40. Y. N. Heit, D.-C. Sergentu, J. Autschbach, Magnetic circular dichroism spectra of transition metal complexes calculated from restricted active space wavefunctions. *Phys. Chem. Chem. Phys.* **21**, 5586–5597 (2019).
41. F. Gendron, V. E. Fleischauer, T. J. Duignan, B. L. Scott, M. W. Löble, S. K. Cary, S. A. Kozimor, H. Bolvin, M. L. Neidig, J. Autschbach, Magnetic circular dichroism of UCl_6^- in the ligand-to-metal charge-transfer spectral region. *Phys. Chem. Chem. Phys.* **19**, 17300–17313 (2017).
42. G. Ganguly, H. D. Ludowieg, J. Autschbach, Ab Initio Study of Vibronic and Magnetic 5f-to-5f and Dipole-Allowed 5f-to-6d and Charge-Transfer Transitions in $[UX_6]^{n-}$ (X = Cl, Br; n = 1, 2). *J. Chem. Theory Comput.* **16**, 5189–5202 (2020).
43. Y. N. Heit, F. Gendron, J. Autschbach, Calculation of Dipole-Forbidden 5f Absorption Spectra of Uranium(V) Hexa-Halide Complexes. *J. Phys. Chem. Lett.* **9**, 887–894 (2018).
44. G. Orlandi, The evaluation of vibronic coupling matrix elements. *Chem. Phys. Lett.* **44**, 277–280 (1976)
45. Becke, A. D. Density–Functional Thermochemistry. III. The Role of Exact Exchange. J. Chem. Phys., 98, 5648–5652 (1993).
46. Dolg, M.; Wedig, U.; Stoll, H.; Preuss, H. Energy-Adjusted Ab Initio Pseudopotentials for the First Row Transition Elements. J. Chem. Phys., 86 (2), 866–872 (1987).
47. Frisch, M. J.; Trucks, G. W.; Schlegel, H. B.; Scuseria, G. E.; Robb, M. A.; Cheeseman, J. R.; Scalmani, G.; Barone, V.; Petersson, G. A.; Nakatsuji, H.; Li, X.; Caricato, M.; Marenich, A. V.; Bloino, J.; Janesko, B. G.; Gomperts, R.; Mennucci, B.; Hratchian, H. P.; Ortiz, J. V.; Izmaylov, A. F.; Sonnenberg, J. L.; Williams-Young, D.; Ding, F.; Lipparini, F.; Egidi, F.; Goings, J.; Peng, B.; Petrone, A.; Henderson, T.; Ranasinghe, D.; Zakrzewski, V. G.; Gao, J.; Rega, N.; Zheng, G.; Liang, W.; Hada, M.; Ehara, M.; Toyota, K.; Fukuda, R.; Hasegawa, J.; Ishida, M.; Nakajima, T.; Honda, Y.; Kitao, O.; Nakai, H.; Vreven, T.; Throssell, K.; Montgomery, J. A., Jr.; Peralta, J. E.; Ogliaro, F.; Bearpark, M. J.; Heyd, J. J.; Brothers, E. N.; Kudin, K. N.; Staroverov, V. N.; Keith, T. A.; Kobayashi, R.; Normand, J.; Raghavachari, K.; Rendell, A. P.; Burant, J. C.; Iyengar, S. S.; Tomasi, J.; Cossi, M.; Millam, J. M.; Klene, M.; Adamo, C.; Cammi, R.; Ochterski, J. W.; Martin, R. L.; Morokuma, K.; Farkas, O.; Foresman, J. B.; Fox, D. J. Gaussian 16 Revision C.01.
48. Korp, J. D.; Bernal, I.; Palmer, R. A.; Robinson, J. C. On the Absolute Configuration of the Tris(ethylenediamine)nickel(II) Cation. I. The Structure and Absolute Configuration of (-)-[Ni(en)_3](NO_3)_2. Acta Crystallographica Section B, 36 (3), 560–564 (1980).
49. Aquilante, F.; Autschbach, J.; Carlson, R. K.; Chibotaru, L. F.; Delcey, M. G.; Vico, L. D.; Fdez. Galván, I.; Ferré, N.; Frutos, L. M.; Gagliardi, L.; Garavelli, M.; Giussani, A.; Hoyer, C. E.; Manni, G. L.; Lischka, H.; Ma, D.; Malmqvist, P.-Å.; Müller, T.; Nenov, A.; Olivucci, M.; Pedersen, T. B.; Peng, D.; Plasser, F.; Pritchard, B.; Reiher, M.; Rivalta, I.; Schapiro, I.; Segarra-Martí, J.; Stenrup, M.; Truhlar, D. G.; Ungur, L.; Valentini, A.; Vancoillie, S.; Veryazov, V.; Vysotskiy, V. P.; Weingart, O.; Zapata, F.; Lindh, R. Molcas 8: New Capabilities for Multiconfigurational Quantum Chemical Calculations Across the Periodic Table. J. Comput. Chem., 37, 506–541 (2016).
50. Hess, B. A. Applicability of the no-pair equation with free-particle projection operators to atomic and molecular structure calculations. Phys. Rev. A 1985, 32, 756–763.
51. Hess, B. A. Relativistic Electronic-Structure Calculations Employing a Two-Component No-Pair Formalism with External-Field Projection Operators. Phys. Rev. A 33, 3742–3748 (1986).
52. Wolf, A.; Reiher, M.; Hess, B. A. The Generalized Douglas-Kroll Transformation. J. Chem. Phys., 117 (20), 9215–9226 (2002).

53. Widmark, P.-O.; Malmqvist, P.-Å.; Roos, B. O. Density-matrix averaged atomic natural orbital (ANO) basis-sets for correlated molecular wave-functions. I. First row atoms. Theor. Chim. Acta, 77, 291–306 (1990).
54. Roos, B. O.; Lindh, R.; Malmqvist, P.-Å.; Veryazov, V.; Widmark, P.-O. Main group atoms and dimers studied with a new relativistic ANO basis set. J. Phys. Chem. A, 108, 2851–2858 (2004).
55. Roos, B. O.; Lindh, R.; Malmqvist, P.-Å.; Veryazov, V.; Widmark, P.-O. New Relativistic Ano Basis Sets for Actinide Atoms. Chem. Phys. Lett. 2005, 409, 295–299.
56. Andersson, K.; Malmqvist, P.-Å.; Roos, B. O. Second-order perturbation theory with a Complete Active Space Self-Consistent Field reference function. J. Chem. Phys., 96, 1218–1226 (1992).
57. Malmqvist, P.-Å.; Roos, B. O.; Schimmelpfennig, B. The Restricted Active Space (Ras) State Interaction Approach with Spin-Orbit Coupling. Chem. Phys. Lett., 357, 230–240 (2002).
58. Mort, J., B. C. and Autschbach, J. Magnitude of Zero–Point Vibrational Corrections to the Optical Rotation in Rigid Organic Molecules: A Time–Dependent Density Functional Study. J. Phys. Chem. A, 109, 8617–8623 (2005).
59. Heit, Y. N.; Gendron, F.; Autschbach, J. Calculation of Dipole-Forbidden 5f Absorption Spectra of Uranium(V) Hexa-Halide Complexes. J. Phys. Chem. Lett. 2018, 9, 887–894.
60. Heit, Y. N.; Gendron, F.; Autschbach, J. Calculation of Dipole-Forbidden 5f Absorption Spectra of Uranium(V) Hexa-Halide Complexes. J. Phys. Chem. Lett., 9, 887–894 (2018).

Acknowledgments

General: We gratefully acknowledge Jérôme Debray (Institut Neél – CNRS & Université Grenoble Alpes) for his crystallographic skills and the tools he developed for crystal indexing and orientation. Dr. David Leboeuf (LNCMI – CNRS) is also acknowledged for the technical assistance in crystal cutting procedures.

Funding: The French National Research Agency (ANR) is acknowledged for financial support through ChiraMolCo (ANR 15-CE29-0006-02), MONAFER (ANR-18-CE09-0032) and MaChiNaCo (ANR-19-CE09-0018) projects. J.A. acknowledges grant CHE-1855470 from the National Science Foundation for supporting the theoretical component of this study. This work was also supported by the CNRS, the University of Bordeaux, the Conseil Régional de la Nouvelle Aquitaine, the European Union's Horizon 2020 research and innovation program under the Marie Sklodowska-Curie grant agreement No 706556 CHIMMM (Postdoctoral fellowship for MC), the Ministry of Higher Education and Research and the LabEX Amadeus.

Author contributions: Investigation, M.A., Á.V.-P., I.B., M.C., P.R; Conceptualization: E.A.H., G.L.J.A.R.; Methodology: M.A., I.B., K.P.; Software: H.L., K.P., J.A.; Formal Analysis: M.A., H.L.; Visualization: M.A.; Writing – Original Draft: M.A.; Writing – Review & Editing, All authors; Supervision: E.A.H., J.A., G.L.J.A.R.; Funding Acquisition: C.T, J.A., E.A.H., G.L.J.A.R.

Competing interests: There are no competing interests to declare.

Data and materials availability: Raw experimental and computational data are available from the corresponding authors upon reasonable request. Developed software for MChD calculations will be released in open-source form within a year from publication.

Figures

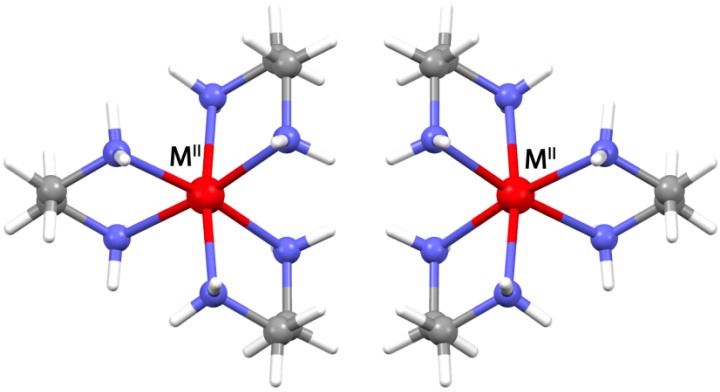

Fig. 1 Molecular structure of the investigated systems. View of the molecular structure of Λ-$[M^{II}(dae)_3]^{2+}$ (left) and Δ-$[M^{II}(dae)_3]^{2+}$ (right) (M^{II} = Ni, Co) complex cations. Color codes: red, M^{II}; blue, N; gray, C; white, H. Nitrate anions are omitted for clarity.

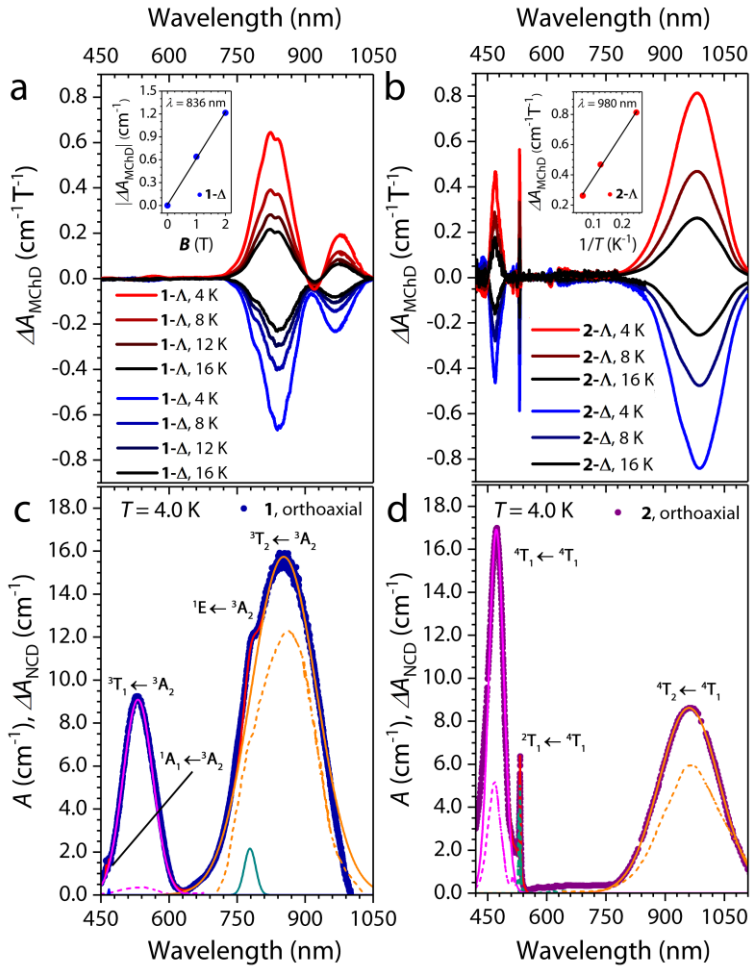

Fig. 2 Experimental MChD, NCD and absorption Spectra. Orthoaxial ΔA_{MChD} spectra for Λ and Δ single crystals of 1 (a) and 2 (b) for several temperatures. The inset in panel *a* shows the MChA strength as a function of the magnetic field strength, the straight line is a fit. The inset in panel *b* shows the MChA strength as a function of the inverse temperature, the straight line is a fit. Absorption spectra (points) versus irradiation wavelength for single crystals of 1 (c) and 2 (d) in orthoaxial configuration. The spectral deconvolution analysis (solid lines) and NCD spectra *T* = 80 K (dashed lines) are also shown.

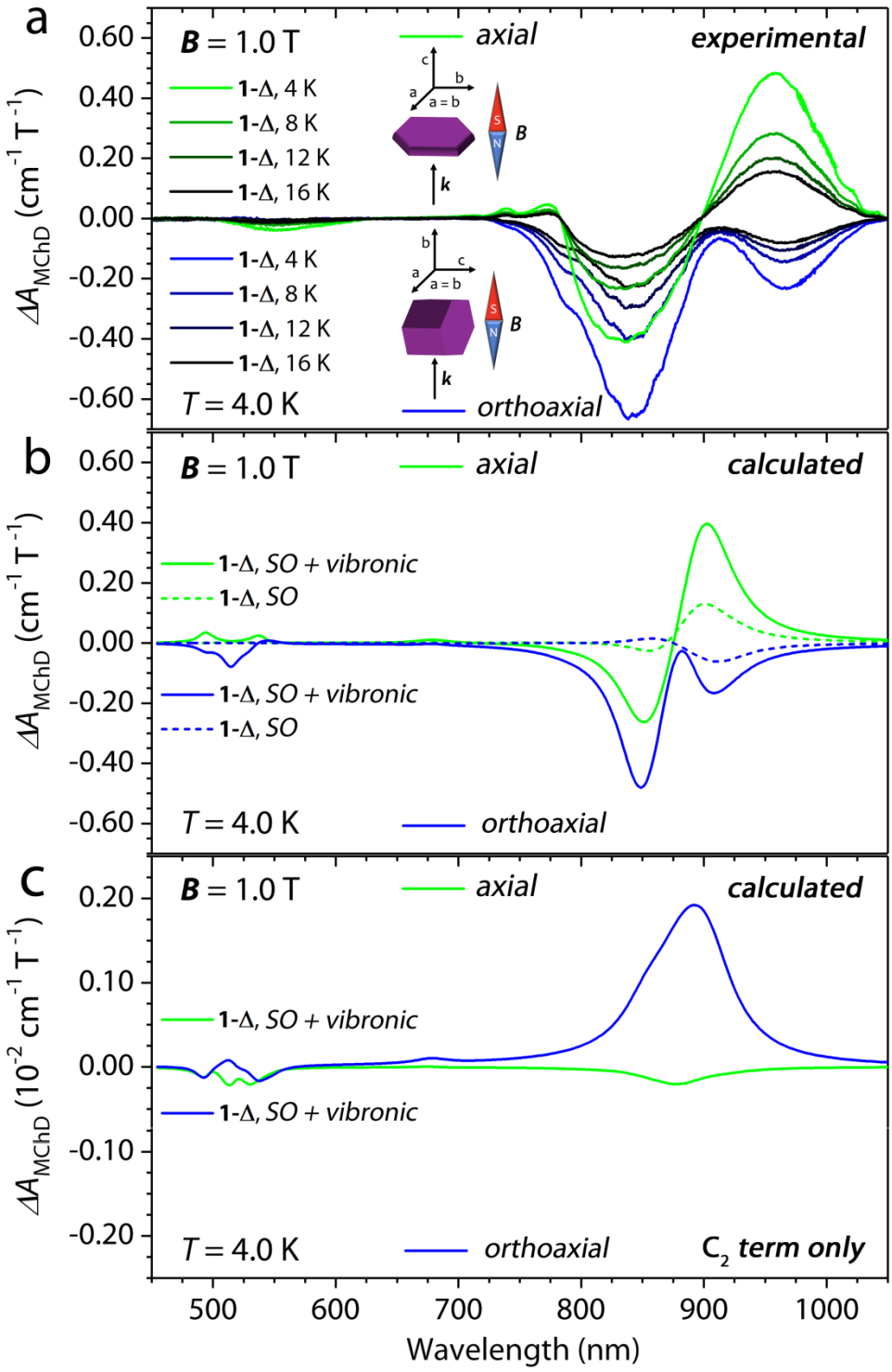

Fig. 3 Comparison between experimental and calculated MChD spectra. Experimental ΔA_{MChD} spectra for a single crystal of 1-Δ in axial and orthoaxial configuration (a), corresponding calculated ΔA_{MChD} spectra (b) and calculated ΔA_{MChD} spectra with only C_2 terms (note change in scale) (c).

583

584 **Table 1. $|\Delta A_{MChD}|$ and absorption coefficients (A) obtained through visible light**
585 **absorption spectroscopy with ($|\Delta A_{MChD}|$) and without (A) applied alternate**
586 **magnetic field on single crystals of compounds 1-Δ and 2-Δ (T = 4.0 K) in**
587 **orthoaxial configuration.**
588

589

Compound	λ (nm)	electronic transition	$\lvert\Delta A_{MChD}\rvert$ (cm^{-1} T^{-1})	A (cm^{-1})	g_{MChD} (T^{-1})
1	967	$^3T_2(^3F) \leftarrow {}^3A_2(^3F)$	0.23	4.48	0.10
	836	$^3T_2(^3F) \leftarrow {}^3A_2(^3F)$	0.66	15.34	0.09
	780	$^1E(^1D) \leftarrow {}^3A_2(^3F)$	N.D.	2.15	N.D.
	530	$^3T_1(^3F) \leftarrow {}^3A_2(^3F)$	0.01	9.08	0.002
	468	$^1A_1(^1G) \leftarrow {}^3A_2(^3F)$	0.00	0.28	0.00
2	960	$^4T_2(^4F) \leftarrow {}^4T_1(^4F)$	0.84	8.70	0.19
	532	$^2T_1(^4P) \leftarrow {}^4T_1(^4F)$	0.59	6.48	0.18
	474	$^4T_1(^4P) \leftarrow {}^4T_1(^4F)$	0.45	17.20	0.05

590

591